

Chapter 13

Cyclic Oxidation

13.1 INTRODUCTION

Alloys used at high temperatures are subjected to duty cycles which vary widely among applications. These range from the rather short operating periods of propulsion engines through the weeks, months or even years of chemical processing or power generation plant campaigns. In all cases, however, start up and shut down involve more or less rapid temperature changes, inducing stresses in the oxide scales which protect the alloys. If no stress relief mechanism is available, the thermally induced strain energy increases with scale thickness. Using the notation of Section 2.10, the stored elastic energy per unit area of scale-alloy interface, W^* , is written as

$$W^* = (1 - v_p)E_{OX}(\Delta T \Delta\alpha)^2 X \quad [13.1]$$

assuming the oxide to be in the linear-elastic regime and present as a thin layer on a much thicker substrate. It is assumed here that the scale is too thin to sustain a temperature gradient, and the stored energy represents thermal mismatch between oxide and metal, not thermal shock to the oxide. If the oxide thickens sufficiently, the strain energy stored in the oxide becomes greater than that required for interface fracture, and the scale spalls [1–4]. The critical stress value which will cause scale spallation depends on the details of the failure mechanism [5,6] and will not be discussed here. Our concern is with the consequences of scale failure and the rate at which breakdown in corrosion protection is arrived at.

A common way of carrying out cyclic oxidation experiments is shown schematically in Fig. 13.1A. Multiple alloy samples are inserted into a furnace and withdrawn again at predetermined intervals using an electric motor drive and automatic timing device. Heating and cooling are quite rapid (Fig. 13.1B), and relatively short cycles can be used. From time to time the experiment is interrupted and the samples withdrawn and weighed. Examples of weight change data accumulated in this way are shown in Fig. 13.2. Since the measured weight changes are the net result of oxygen weight uptake due to scaling plus any internal oxidation, and weight losses due to metal oxide spallation, the interpretation of results like these is not simple. However, the technique is economical and has become popular as a way of generating

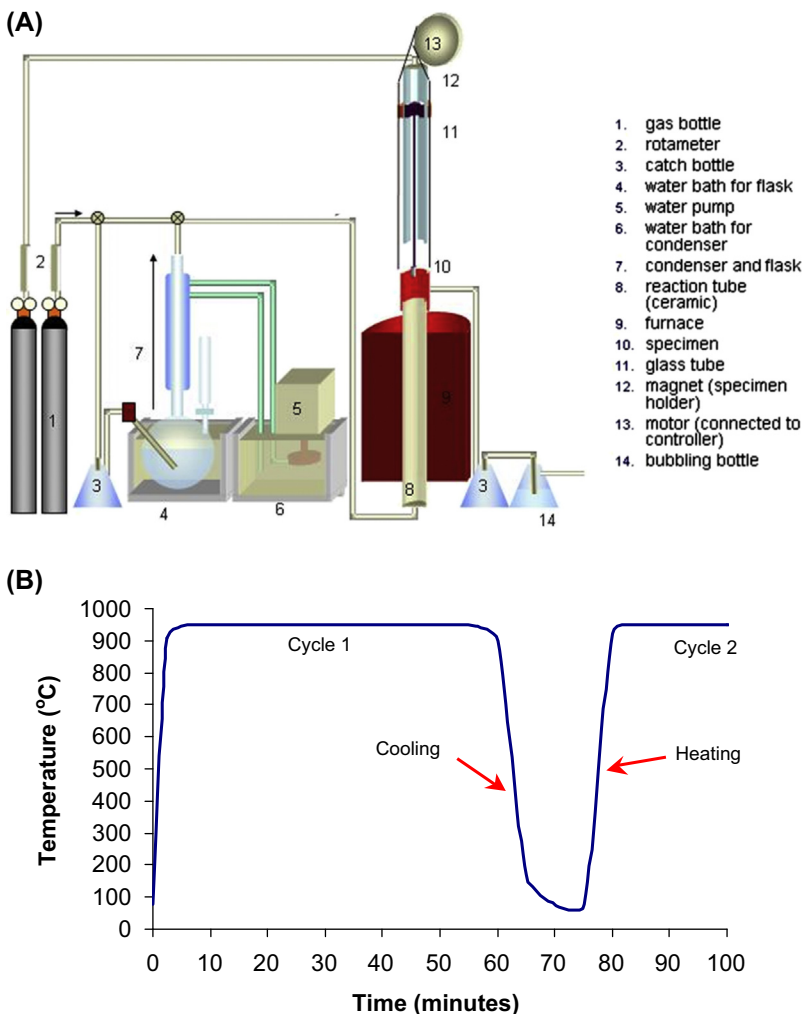


FIGURE 13.1 (A) Experimental apparatus for cyclic oxidation and (B) observed temperature-time trajectories at specimen surfaces.

comparative alloy performance data under more-or-less realistic exposure conditions.

One way of overcoming the interpretation problem is to capture spalled oxide and weigh it together with the sample. The resulting ‘gross mass gain’ is shown plotted for some FeCrAl alloys in Fig. 13.3, where it is compared with ‘net mass gains’, ie, the changes in weight of the reacted samples after loss of spalled oxide. Whilst the onset of spallation is clear in the case of PM2000, it is obscured in the case of APM and JA13 by the continuing positive net mass

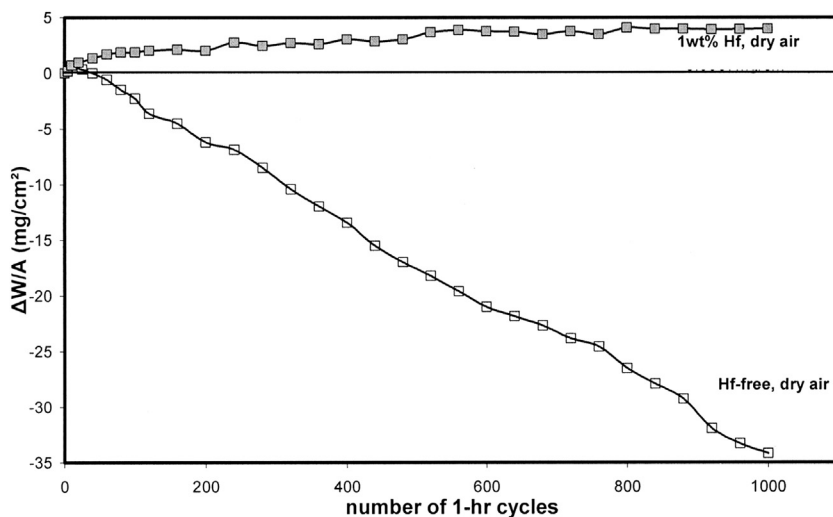


FIGURE 13.2 Cyclic oxidation weight change data for β -Ni-50Al in dry air at 1200°C.

gains. Measurement of spalled oxide makes the position clear, but the experiment presents practical difficulties.

Spalled oxide is collected by holding reacting alloys in inert, refractory crucibles. Because spallation can cause the violent ejection of oxide particles, the crucibles should be fitted with lids. Such an arrangement impedes mass transfer between the specimen and gas flowing past the crucible and is therefore not suited to the use of mixed gases. An alternative method for observing spallation directly is the use of continuous thermogravimetric analysis (CTGA).

In the CTGA experiment, a microbalance is used to record weight changes during the entire process, cycle after cycle. Thus oxidation kinetics are observed directly during the high temperature periods, and abrupt weight losses corresponding to scale spallation are, at least in principle, observable. The technique was reported by Pivin et al. [8], Christ et al. [9,10] and Vangeli [11]. An example of the resulting data is shown in Fig. 13.4. Because only one sample can be attached to the microbalance, the instrument is committed for hundreds or even thousands of hours, and the technique is expensive. Monceau et al. [12,13] have described modifications to the technique designed to improve productivity by fitting multiple microbalances to a single, temperature cycling apparatus.

Partial or complete spallation means that the average scale thickness is decreased. Because scale growth is usually diffusion controlled,

$$\frac{d(\Delta W/A)}{dt} = \frac{\bar{k}_w}{\Delta W/A} \quad [13.2]$$

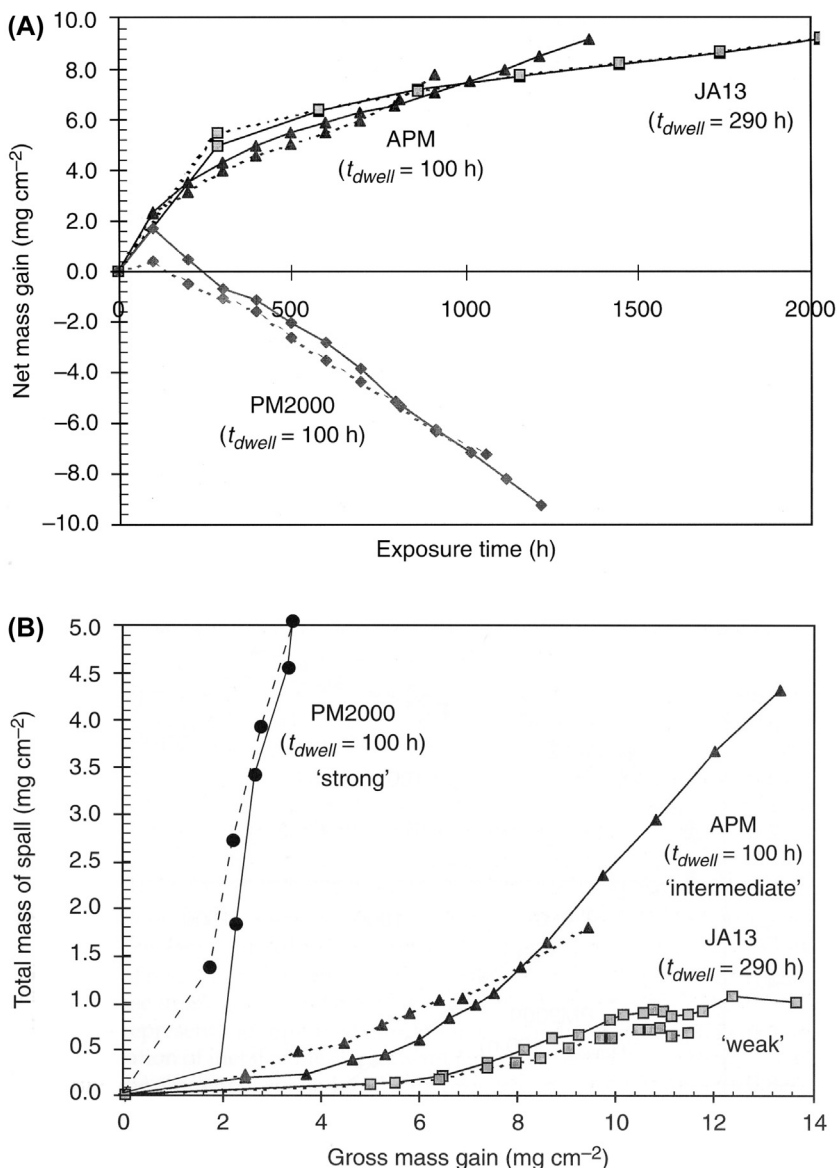


FIGURE 13.3 (A) Net mass gain and (B) spalled oxide mass for FeCrAl alloys oxidised in air at 1300°C [7]. Published with permission from IOM Communications.

and the rate of weight uptake averaged over multiple scale segments of different thickness, is consequently greater. The effect is illustrated in Fig. 13.4, where the oxidation rate during high-temperature cycles is seen to be higher than rates observed during isothermal exposure for the same total time. Thus the value of \bar{k}_w cannot be related to the isothermal k_w value

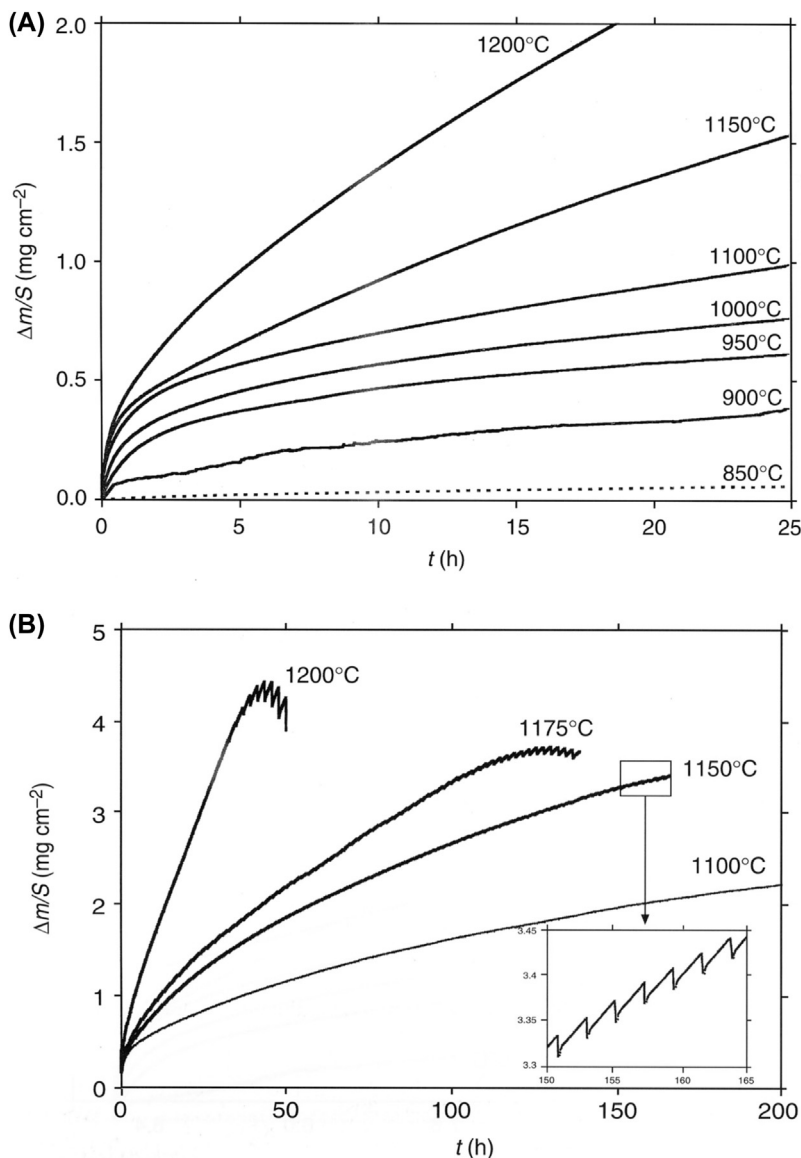


FIGURE 13.4 Continuous thermogravimetric analysis results obtained during (A) isothermal and (B) cyclic oxidation of 353 MA in air. *With permission from P. Vangeli, Ref. 7, p. 198, IOM Communications Ltd.*

without knowledge of the spallation process. The practical result is that the alloy is consumed more rapidly.

Cyclic oxidation testing is intended to provide information on alloy service lifetimes. The definition of lifetime will depend on alloy functionality. If spallation leads to consequential and irreparable damage such as the loss of an

adhering thermal barrier coating (Fig. 1.6), then lifetime can be defined as time to reach a certain fraction of surface area affected. In other cases, lifetime is usually defined as the time at which the alloy loses the capacity to ‘reheal’ by reforming its protective oxide scale. Subsequent alloy degradation is rapid as a result of either fast oxidation of the alloy base metal or attack on the unprotected alloy by secondary corrodents. The processes leading to the onset of this failure form the focus of the present chapter.

We consider first the diffusion controlled depletion of protective scale-forming metal within the alloy, and the way in which this is accelerated by spallation and rehealing. In order to make use of this analysis, it is then necessary to describe the kinetics of scale growth during repeated spallation. Models which have been developed for this purpose are then combined with the subsurface depletion description to arrive at lifetime predictions. Finally, the effects of experimental variables, in particular gas composition, on the results of cyclic oxidation exposures are reviewed. Attention is focused on alumina and chromia-forming alloys.

13.2 ALLOY DEPLETION AND SCALE REHEALING

The selective oxidation of chromium or aluminium removes metal from the alloy subsurface region. The resulting concentration profile for the reacting metal is obtained by solving the diffusion equation (Fick’s Second Law) for that alloy component. In the steady-state, where the scale-alloy interfacial concentration is time-independent, Wagner’s analysis (Section 5.4) leads to the general solution (Eq. [5.25]). If interface recession is slow, as is the case for slow-growing chromia and alumina, the interfacial concentration of reacting element B, $N_{B,i}$, becomes

$$N_{B,i} = \frac{N_B^{(o)} - \varphi}{1 - \varphi} \quad [13.3]$$

where $\varphi = ((\pi k_c)/2\tilde{D})^{1/2}$ with \tilde{D} the alloy interdiffusion coefficient, k_c the rate constant defined in (Eq. [1.28]), and $N_B^{(o)}$ original alloy concentration.

Whittle [14] analysed the conditions under which an alloy could reform its protective scale after a spallation event in which the entire scale was lost. This treatment ignored transient oxidation, applying Eq. [13.3] to the first oxidation cycle, and enquired into the further depletion of metal B on the assumption that scale growth followed the same parabolic kinetics as in the first cycle. The model is shown schematically in Fig. 13.5. A qualitative understanding of the situation can be arrived at from a consideration of the mass balance for B at the scale-alloy interface. After spallation at $t = t^*$, scale growth is assumed to recommence at the same rapid rate as at the beginning of the first cycle, causing the maximum rate of B withdrawal from the alloy. However, the chemical potential gradient of B at $t = t^*$ is capable of delivering B to the interface only at the slow rate in effect at the end of the preceding cycle. The two possibilities are that BO_v fails to reform, or that $N_{B,i}$ is further reduced to the point where

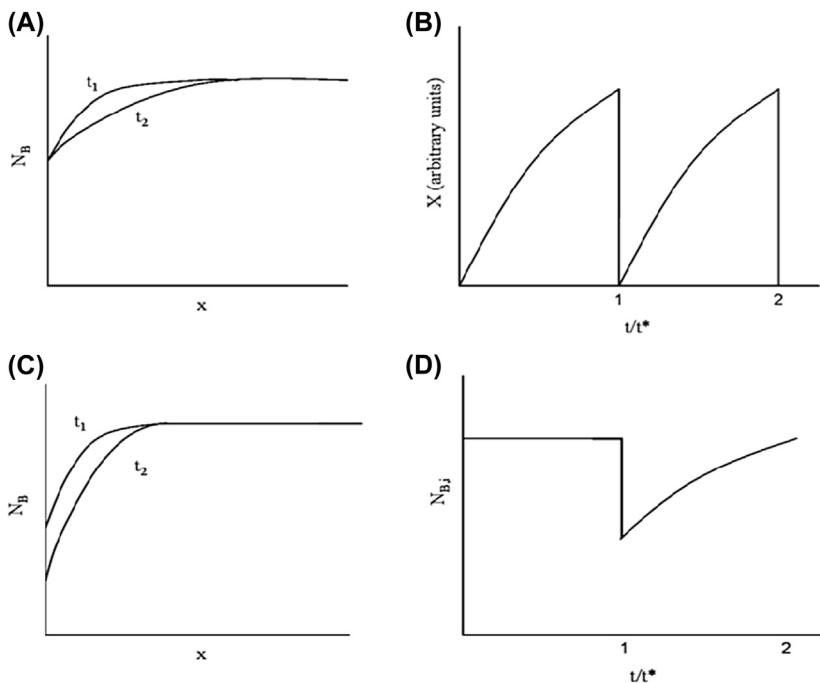


FIGURE 13.5 Whittle's cyclic oxidation model: (A) depletion profiles during steady-state isothermal oxidation, $t_2 > t_1$, (B) successive scale growth cycles for 100% spallation at $t = t^*$, (C) depletion profiles, $t_1 < t^* < t_2$, and (D) recovery of interfacial concentration after rehealing. With kind permission from D.P. Whittle, *Oxid. Met.* 4 (1972) 171, Springer Science and Business Media.

the gradient in B is increased sufficiently to drive the required flux from the alloy to the interface. In the latter case, scale growth slows with time, and the flux of B from the alloy allows the value of $N_{B,i}$ to increase. Eventually, if the cycle is long enough, steady-state conditions are restored.

A quantitative description requires solution of Fick's Second Law using, as an initial condition, the profile in $N_{B,i}$ at $t = t^*$, and a new formulation of the interfacial mass balance:

$$(1 - N_{B,i}(t)) \left[k_c / 2(t - t^*)^{1/2} \right]^{1/2} = D \frac{\partial N_B}{\partial x} \quad [13.4]$$

which replaces (Eq. [5.24]). Because scale growth is assumed parabolic with $(t - t^*)$, it is not parabolic with t , and a time-dependent interfacial concentration results. No exact analytical solution was possible. Instead, an approximate solution was found and verified by numerical analysis [15]. This led to an expression for the time dependence of $N_{B,i}$ for $t > t^*$

$$N_{B,i} = \frac{\varphi}{1 - \varphi} \left[N_B^{(o)} - \varphi - \frac{\varphi}{1 - \varphi} \left(1 - N_B^{(o)} \right) \frac{2}{\pi} \sin^{-1} (t/t^*)^{1/2} \right] \quad [13.5]$$

The form of this result is illustrated in Fig. 13.5D. The interfacial concentration is seen to drop instantaneously to a lower value, then slowly recover. Depletion profiles before and after this spallation event are compared in Fig. 13.5C. As time passes, $N_{B,i}$ increases until it reaches the steady-state value $N_{B,i}^S$. The depletion depth is then greater, as would also result from isothermal oxidation for a sufficiently long time (Fig. 13.5A).

The criterion used for protective scale formation was Wagner's condition that sufficient flux of B is available to maintain exclusive B oxide scale growth. The minimum initial $N_B^{(o)}$ value, $N_{B,min}^I = \varphi$, is calculated for the first cycle from Eq. [5.22] by setting $N_{B,i} \approx 0$

$$N_{B,min}^I = \varphi \quad [13.6]$$

At any lower initial concentration, the interface concentration necessary to produce a sufficient flux of B in the alloy to sustain scale growth is less than zero, and exclusive BO_v growth therefore ceases. Applying the same criterion after the first spallation event leads to the requirement that $N_{B,min}$ be large enough to keep $N_{B,i} > 0$ at $t = t^*$. From Eq. [13.5] we find

$$(1 - \varphi)N_{B,i}(t^*) = N_B^{(o)} - \varphi - \frac{\varphi}{1 - \varphi} (1 - N_B^{(o)}) \quad [13.7]$$

and it follows that the condition for $N_{B,i}(t^*) > 0$ is

$$N_B^{(o)} \geq N_{B,min}^{II} = 1 - (1 - \varphi)^2 \quad [13.8]$$

where the superscript II signifies the value necessary to sustain exclusive B oxidation in a second cycle. Whittle extended the analysis to a third cycle by using the criterion $N_{B,i}(t^*) \geq \varphi$. Thus it was proposed that the interfacial concentration after the first spallation and rehealing event was not only greater than zero, as required to grow the second scale, but needed to be sufficient to grow a third scale when required. Application of this criterion to Eq. [13.5] yields

$$(\varphi/1 - \varphi) \left[N_B^{(o)} - \varphi - [\varphi/(1 - \varphi)] (1 - N_B^{(o)}) \right] \geq \varphi \quad [13.9]$$

and hence

$$N_{B,min}^{III} > 1 - (1 - \varphi)^3 \quad [13.10]$$

Whittle also suggested that [Eq. [13.10]] would provide an estimate of the required $N_{B,min}$ to reheat after further cycling. However, as pointed out by Nesbitt [16], this requires significant recovery in the value of $N_{B,i}$ between cycles, and this would not be available for regular cycles of period t^* . In fact, Eq. [13.5] predicts that $N_{B,i}$ recovers to only about 50% of its former value in the time from t^* to $2t^*$.

Wahl [17] adopted a different approach in order to extend the analysis to greater numbers of cycles, assuming no recovery in $N_{B,i}$ at all. As a result, the value of the interfacial concentration decreases in a stepwise fashion with the decrease after each spallation event given by

$$N_{B,i(\text{Before})} - N_{B,i(\text{After})} = (1 - N_{B,i(\text{After})})\varphi \quad [13.11]$$

For an alloy to survive for n cycles, it needs a value of $N_{B,i(\text{After})} \geq \varphi$ for cycle $(n - 1)$. Using Eq. [13.11] to count back through all n steps, it is found that the required starting concentration $N_{B,\min}^N$ is given by

$$N_{B,\min}^N = 1 - (1 - \varphi)^n \quad [13.12]$$

Thus agreement was achieved with Whittle's calculations for $n = 2$ and 3. However, because of the assumed lack of recovery in interfacial concentration, the maximum number of cycles an alloy can withstand is predicted to be unrealistically small.

Nesbitt [16] proposed a combination of the Whittle and Wahl models. As shown by Whittle's Eq. Eq. [13.5], the recovery in each regular cycle amounts to 50% of the value at the end of the previous cycle. Assuming that the decrease in $N_{B,i}$ immediately after each spallation is φ , then the net decrease for each full cycle is $\varphi/2$. Applying this to Wahl's Eq. [13.12] then yields the result

$$N_{B,\min}^N = 1 - (1 - \varphi/2)^n + \varphi/2 \quad [13.13]$$

Unrealistically short lifetimes are still predicted.

The main reason all of these models fail is their simplistic, and unduly pessimistic, assumption that all of the scale spalls at every cycle, and the alloy therefore needs to regrow a complete new scale. This amounts to a rather rapid average linear rate constant for alloy consumption and is quite unrepresentative of practical alloys. As seen in Fig. 13.6, spallation from even a susceptible material like undoped β -NiAl is incomplete. To deal with this reality, it is necessary to devise better spallation models.

13.3 SPALLATION MODELS

One purpose of cyclic oxidation testing is to collect comparative alloy performance data relatively quickly and use it to predict lifetimes which can be very lengthy under service conditions. In order to extrapolate from the accelerated laboratory test to operating performance, one needs a way of relating spallation and rehealing behaviour to experimental conditions. The spallation models attempt to provide a basis for the necessary relationships.

Smialek [18] proposed a cyclic stepwise partial spallation model to account for the cyclic oxidation behaviour of undoped β -Ni-42Al (atom percent)

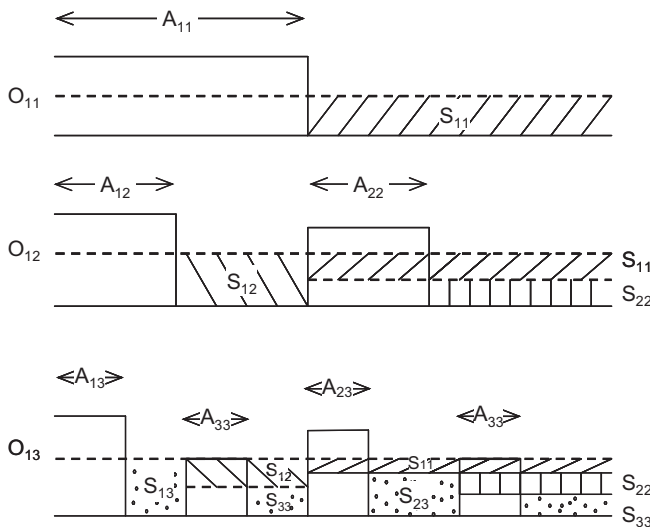


FIGURE 13.6 Schematic representation of Smialek's spalling model [18]. Dashed line shows original alloy surface. Subsequent alloy-scale interface represented as flat for simplicity.

at 1100°C. The basic assumptions were that spallation occurred only at the oxide-alloy interface, that a constant area fraction of all oxide segments still present spalled during each cooling cycle and that oxidation kinetics were parabolic. A schematic view of the reaction cross-section is shown in Fig. 13.6, where the subscripts denote the following: m is the cycle number at which the oxide segment commenced growth, j is the cycle number at which it spalled and n in the total number of cycles so far. The surface area fractions of intact oxide are A_{mn} , containing oxygen weights of X_{mn} per unit area. These contribute $O_{mn} = X_{mn}A_{mn}$ mass of oxygen per unit sample area, so that the total oxygen uptake on a sample after n cycles is

$$W_o/A = \sum_{m=1}^n O_{mn} \quad [13.14]$$

Shaded portions in the diagram represent parts of oxide which have spalled and where, consequently, metal has been lost. The metal loss corresponding to each lost metal oxide segment is denoted by S_{mj} . The total loss per unit sample area sustained in cycle j is accordingly $\sum_{m=1}^j S_{mj}$. The total loss accumulated by the n th cycle is therefore

$$W_M/A = \sum_{j=1}^n \sum_{m=1}^j S_{mj} \quad [13.15]$$

The metal losses are related to the spalled oxide losses via

$$S_{mj} = 1.125 X_{mj} A_{mj} \quad [13.16]$$

where 1.125 is the ratio of metal to oxygen weights in Al_2O_3 , and X_{mj} represents the weight of oxygen per unit area in spalled segments making up fractional areas A_{mj} .

The spallation model in Fig. 13.6 represents a fixed spallation fraction, k_s , and the oxide (of varying thicknesses) covers a sample surface area fraction of $(1 - k_s)$. Different fractions of remnant oxide have differing histories:

$$A_{1n} = (1 - k_s)^n \quad m = 1 \quad [13.17]$$

$$A_{mn} = (1 - k_s)^{n-(m-1)} k_s \quad m \geq 2$$

The thicknesses of these regions are determined by their existence time $\Delta t(n - m + 1)$, where Δt is the duration of each cycle. Thus

$$X_{mn}^2 = 2k_w \Delta t(n - m + 1) \quad [13.18]$$

and a combination of Eqs [13.14], [13.17] and [13.18] leads to

$$W_o/A = (2k_w \Delta t)^{\frac{1}{2}} (1 - k_s)^n \left[1 + k_s \sum_{m=2}^n (n - m + 1)^{\frac{1}{2}} (1 - k_s)^{1-m} \right] \quad [13.19]$$

A similar accounting yields an estimate of the metal loss

$$W_M/A = 1.125 (2k_w \Delta t)^{\frac{1}{2}} k_s \sum_{i=1}^n \sqrt{i} (1 + (n - i)k_s) (1 - k_s)^{i-1} \quad [13.20]$$

and the net weight uptake is then

$$\Delta W/A = W_o/A - W_M/A \quad [13.21]$$

No closed form solutions were found, and numerical computation was necessary.

An investigation [18] of the form of $\Delta W/A$ versus n curves and their dependence on the parameters k_w , k_s and Δt was fruitful. The general form of the predicted curve is shown in Fig. 13.7. It is seen to be of the same form as those observed experimentally (Figs. 13.2, 13.3A and 13.11A). The initial increase in weight is due to the rapid scaling observed at short times, and as exposure time increases, the parabolic scaling rate slows. However, if a constant fraction of the scale spalls at each cycle, the weight lost during each cycle increases with scale thickness and elapsed time. This causes the net weight change to become negative. Any resulting decrease in average scale thickness leads to an increase in scaling rate (Eq. [13.2]), and a balance is struck between scale growth and scale loss. Spalled fragments contain metal as well as

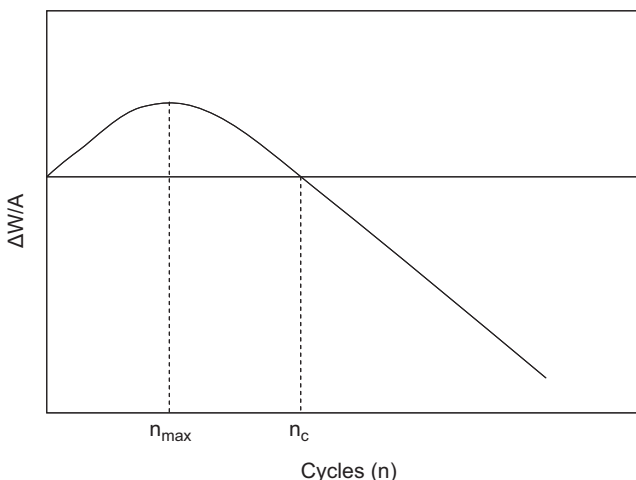


FIGURE 13.7 Net specimen weight changes predicted from Eqs [13.19]–[13–21].

oxygen, and a steady-state net weight loss results. The aim of the spallation models is to describe the onset and subsequent rate of this metal depleting process.

The numbers of cycles required to reach the maximum weight gain n_{\max} , and to reach the crossover between positive and negative net weight change, n_c , were both found to depend on the quantity $(1 - k_s)/k_s$, and n_{\max}/n_c was equal to 0.3. Comparison of the model with experimental data in Fig. 13.8 [19]

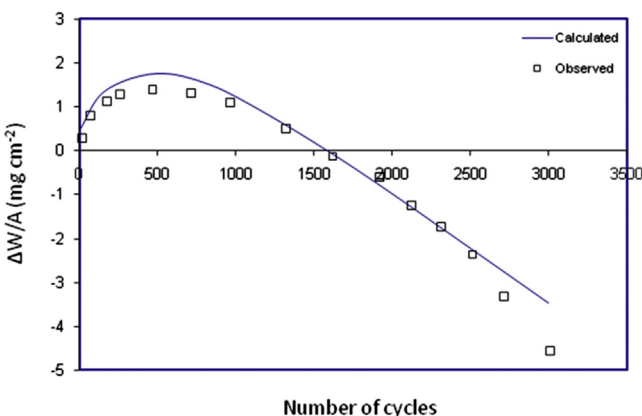


FIGURE 13.8 Fit provided by model of Eqs [13.18]–[13.21] for cyclic oxidation data for NiCrAlZr at 1200°C. Model uses isothermally measured k_w and $Q_O = 10^{-4}$. Published with permission from C.E. Lowell, J.L. Smialek, C.A. Barrett, in: R.A. Rapp (Ed.), *High Temperature Corrosion*, NACE, Houston, TX (1983), p. 219, © NACE International 1983.

TABLE 13.1 Application of Spalling Model of Smialek [18] to Data for Ni-42Al at 1100°C

Δt (h)	k_w ($\text{mg}^2 \text{cm}^{-4} \text{h}^{-1}$)	k_s
1	0.0026	0.0016
20	0.0020	0.1225
50	0.0036	0.1225

for NiCrAlZr subjected to one-hour cycles at 1200°C shows a satisfactory fit over 2000 cycles, during which the alloy continued to regrow alumina. The reason the alloy resisted depletion so well was the small amount of scale spalled at each cycle. Fitting the model to observed $\Delta W/A$ versus n curves yielded realistic assessments of k_w and the result $k_s \approx 0.002$. However, as seen in Table 13.1, the value of k_s estimated for Ni-42Al by curve fitting increases substantially for longer cycle times. Direct measurement of k_s by examination of spalled specimens showed that in fact k_s varied widely, from 0.004 to 0.195. It is therefore concluded that indeed $k_s \ll 1$, thereby accounting for the early failure of the Whittle and Wahl models. However, it must also be concluded that the assumption of a constant k_s value was incorrect. Further examination of the data showed that k_s increased with average oxide thickness, as would be expected from Eq. [13.1].

The spalling model was subsequently developed further by Lowell et al. [19–21] to take account of this variation in k_s . An empirical spalling constant, Q_o , was used to relate the fraction of scale spalled to its average thickness (or weight per unit sample area, W_r) at the end of the preceding high temperature cycle:

$$k_s = Q_o W_r^\alpha \quad [13.22]$$

The exponent α is an experimental constant, usually found to be close to unity. Examples of this relationship are shown in Fig. 13.9. The weight of oxide spalled is in this case

$$W_s = Q_o W_r^2 \quad [13.23]$$

Because the amount spalled increases with oxide thickness, a pseudo-steady-state is reached in which the amount of oxide lost in each cycle is equal to the amount grown in the previous cycle (Fig. 13.10). Under these conditions, the overall rate at which scale-forming metal is lost becomes linear. Thus the more-or-less linear rate of specimen weight loss in the later stages of thermal cycling exposure (eg, Fig. 13.3) is explained. The model has become known as COSP (Cyclic Oxidation Spalling Program) and is

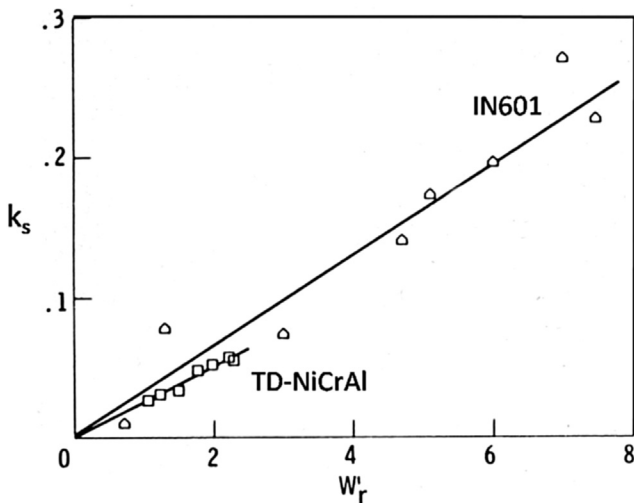


FIGURE 13.9 Dependence of spall fraction on weight uptake for IN601 forming Cr_2O_3 at 1100°C and TD-NiCrAl forming Al_2O_3 at 1200°C [19]. Published with permission from C.E. Lowell, J.L. Smialek, C.A. Barrett, in: R.A. Rapp (Ed.), *High Temperature Corrosion*, NACE, Houston, TX (1983), p. 219, © NACE International 1983.

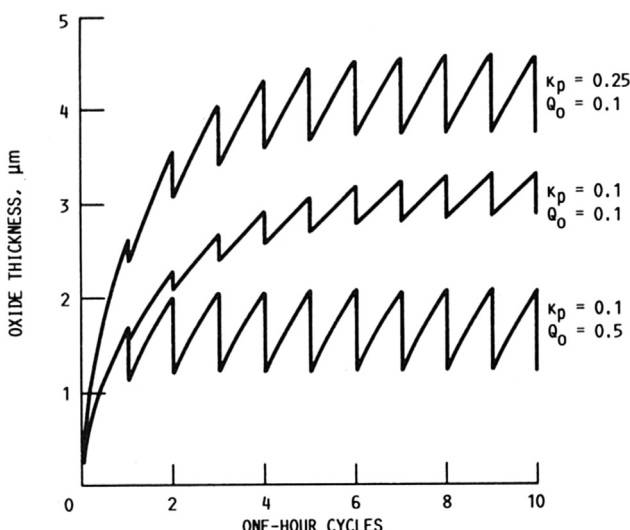


FIGURE 13.10 Predictions of the Lowell et al. [19–21] spalling model for time dependence of average scale thickness and rate of scale-forming metal consumption. Reproduced from J.A. Nesbitt, *J. Electrochem. Soc.* 136 (1989) 1518, with permission of The Electrochemical Society.

available as a computer program [22]. A variety of partial spall distributions is available within this program.

The predictions of this model have been summarised by its authors [23]. For a given oxide,

$$n_{\max} \propto (k_w \Delta t Q_o^2)^{-\frac{1}{3}} \quad [13.24]$$

$$n_c \approx 3.3 n_{\max} \quad [13.25]$$

$$(\Delta W/A)_{\max} \propto (k_w \Delta t / Q_o)^{\frac{1}{3}} \quad [13.26]$$

and the final linear mass loss rate

$$\left(\frac{d(W/A)}{dt} \right)_{Final} \propto \left(\frac{k_w Q_o}{\Delta t} \right)^{\frac{1}{3}} \quad [13.27]$$

As seen in Fig. 13.11, very good fits to net weight change data can be achieved with this model. However, although the effects of cycle frequency are well predicted for this chromia former, they are only approximately correct for the alumina former MA 956 (Y_2O_3 dispersed FeCrAlY) [23] and unsuccessful for Zr-doped NiAl [24].

Modifications to these spalling models have been suggested. Evans et al. [2,25] have proposed that the quantity of spalled oxide is given by

$$W_s = A W_r + B (W_r \Delta T)^2 + C (W_r^3 \Delta T^4) + D (W_r^4 \Delta T^6) \quad [13.28]$$

or, more simply, by

$$k_s = \left(\frac{W_r \Delta T^2}{\beta} \right)^m \quad [13.29]$$

In these expressions, $W_r \Delta T^2$ represents the elastic energy in the oxide resulting from rapid cooling (Eq. [13.1]), β depends on the strength of the scale-metal interface and m reflects the mechanical properties of the oxide. Similarly, Chan [26] proposed that

$$W_s \propto \Delta T^2 (W_r)^{m+1} \quad [13.30]$$

Finally, the Smialek model of Fig. 13.6 has been revisited by Poquillon and Monceau [27], who found a new solution for the amount of oxide grown in the n th cycle,

$$\Delta W_o(n) = (2 k_w \Delta t)^{\frac{1}{2}} \left[k_s \sum_{j=1}^{n-1} (1 - k_s)^{j-1} \left(\sqrt{j} - \sqrt{j-1} \right) + (1 - k_s)^{n-1} \left(\sqrt{n} - \sqrt{n-1} \right) \right] \quad [13.31]$$

where the index j defines the cycle in which spallation occurs. They showed analytically that in the limit as n becomes very large

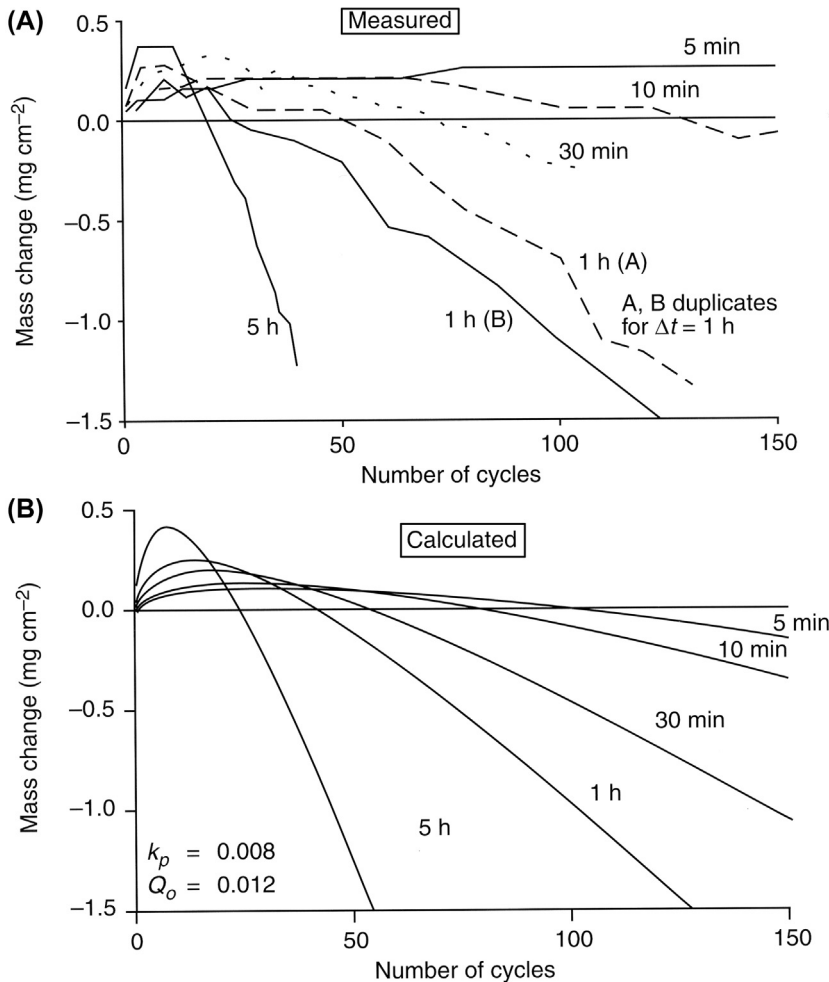


FIGURE 13.11 Effect of cycle duration on cyclic weight changes for Ni-30Cr oxidised at 1050°C: (A) measured, (B) calculated. With kind permission from C.E. Lowell, C.A. Barret, R.W. Palmer, J.V. Auping, H.B. Probst, *Oxid. Met.* 36 (1991) 81, Springer Science and Business Media.

$$\Delta W_o(\infty) = (2k_w \Delta t)^{\frac{1}{2}} k_s [\text{Li}_{-1/2}(z) - z \text{Li}_{-1/2}(z)] \quad [13.32]$$

where $z = 1 - k_s$ and $\text{Li}_n(z)$ is the polylogarithmic function

$$\text{Li}_n(z) = \sum_{j=1}^{\infty} \frac{z^j}{j^n} \quad [13.33]$$

For $0 < k_s < 1$, Eq. [13.33] converges to a limit, representing a constant oxidation weight gain per cycle. This, of course, represents a constant rate of

metal loss and is analogous to the COSP Eq. [13.27]. It depends in a straightforward way on k_w and Δt , but in a complex way on k_s , which appears in the $Li_n(z)$ function.

Poquillon and Monceau [27] tested the applicability of their spallation model to experimental weight change data for the cyclic oxidation of a series of alumina-forming alloys. To do this, they treated the rate constant k_w and the spallation constant k_s as adjustable parameters, minimising the residual error between calculated and measured values

$$\text{Error}(k_w, k_s) = \sum_{i=1}^{\infty} [\Delta W_i(\text{calc}) - \Delta W_i(\text{exp})]^2$$

over each set of n data points. Very good fits were obtained, and the results are summarised in Table 13.2 for binary Ni-Al alloys oxidised in one-hour cycles at 1150°C. Reasonable agreement between measured and calculated values was found for both n_{\max} and n_c . In agreement with the COSP model, $n_c \approx 3:3 n_{\max}$. Importantly, the values of k_w and k_s arrived at in minimising the error in the fit were also consistent with the steady-state rates of weight loss observed in the long-term.

As we have seen, the spallation models appear to provide self-consistent descriptions of the major features of cyclic oxidation weight-change kinetics, in at least some cases. To predict the lifetime of an alloy (ie, the exposure limit beyond which the alloy can no longer redevelop its protective scale), we need to relate spallation to the depletion in scale-forming metal.

13.4 COMBINATION OF SPALLING AND DEPLETION MODELS

Nesbitt [16] used the spalling model of Eq. [13.23] together with the computational approach of Eqs [13.19]–[13.21] to calculate the rate at which the scale-forming element is withdrawn from the alloy. For an oxygen uptake rate given by Eq. [13.2], and an oxide of stoichiometry MO_v , the corresponding rate of metal consumption is

$$\frac{d(W_M/A)}{dt} = \frac{m_M}{16v} \frac{k_w}{W_o/A} \quad [13.34]$$

This statement of metal flux out of the alloy surface can be used in the mass balance Eq. [5.29] to provide a boundary condition for the alloy diffusion problem. Nesbitt applied this approach to the ternary Ni-Cr-Al system, using multicomponent diffusion equations of the form Eq. [2.115]. To deal with the necessarily time-dependent values of $N_{\text{Al},i}$ and $N_{\text{Cr},i}$, as well as the concentration dependence of the D_{ij} , a finite difference calculation was employed. The description was applied to cyclic oxidation of Zr-doped alumina-forming Ni-Cr-Al alloys [28]. As seen in Fig. 13.12, use of the fractional spallation model

TABLE 13.2 Application of Spalling Model of Pocquillon and Monceau [27] to Oxidation at 1150°C in One-Hour Cycles

Alloy (at. %)	n_{\max}		n_c		$10^6 k_w (\text{mg}^2 \text{ cm}^{-4} \text{ s}^{-1})$	$k_s (\%)$
	Experimental	Calculated	Experimental	Calculated		
Ni-45Al	9–115	23	9–115	73	2.5	0.48
Ni-47Al	37–69	64	166–240	221	3.7	0.54
Ni-51.2Al	41–55	75	147–198	249	1.6	1.55

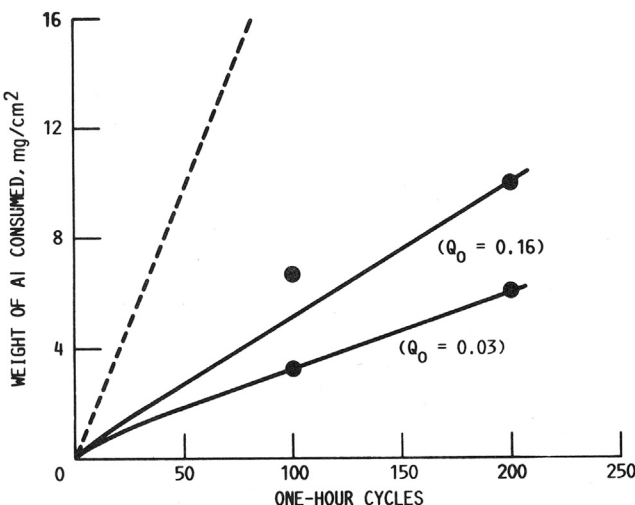


FIGURE 13.12 Aluminium consumption during cyclic oxidation of Ni-Cr-Al(Zr) at 1200°C: points—measured; dashed line, Whittle and Wahl analysis; continuous lines, Nesbitt analysis. Reproduced from J.A. Nesbitt, *J. Electrochem. Soc.* 136 (1989) 1518, with permission of The Electrochemical Society.

(Eqs [13.23]–[13.37]) led to an estimate of aluminium depletion which was much more realistic than the 100% spallation model of Whittle and Wahl. We conclude from this success that the COSP spallation model of Eqs [13.23]–[13.27] combined with an accurate calculation of subsurface alloy depletion correctly describes the consumption of protective scale-forming metal in the early stages of reaction.

Lifetime predictions for these alloys were only partially successful. The diffusion analysis was used to predict the value of $N_{\text{Al},\text{min}}$ required to survive 200 cycles of one-hour duration at 1200°C before $N_{\text{Al},i}$ was depleted to zero. As seen in Fig. 13.13, reasonable agreement with experimental findings [29] was achieved for high $N_{\text{Cr}}^{(0)}$ values, but not for low chromium levels. This failure was attributed to the neglect of transient oxidation, the consequences of which would become more serious as aluminium depletion progressed with further cycling. The presence of chromium was thought to suppress the extent of transient oxidation, thereby rendering the model a more realistic description.

Li and Gleeson [30] have carried out a somewhat similar analysis for the cyclic oxidation at 1000°C of the chromia-forming alloy 800HT (a heat-treated version of alloy 800 (Table 5.1)). The COSP treatment of spallation was used to obtain a value for the spalling constant Q_0 , and a finite difference

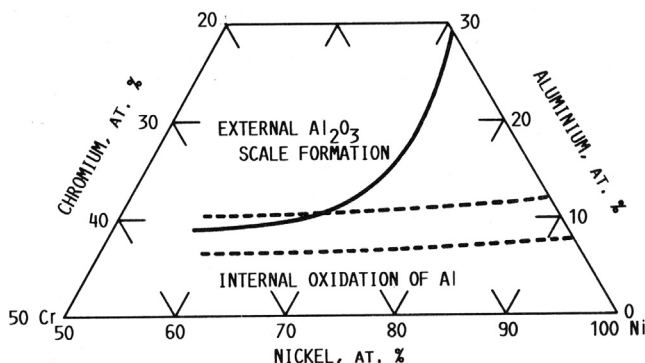


FIGURE 13.13 Experimental (continuous curve) and predicted (dashed lines) alloy aluminium levels necessary for rehealing Al_2O_3 scales on Ni-Cr-Al + Zr over 200 one-hour cycles at 1200°C. Reproduced from J.A. Nesbitt, *J. Electrochem. Soc.* 136 (1989) 1518, with permission of The Electrochemical Society.

technique employed to model the nonsteady-state alloy diffusion process. However, this was simplified by treating the alloy as a quasi-binary, ie, by setting $D_{ij}(i \neq j) = 0$. Diffusion coefficient values were estimated by applying the Boltzmann-Matano Eq. [2.142] to a measured chromium concentration profile and calculating an average \bar{D}_{Cr} for the range of concentrations involved. This procedure was validated by comparing predicted and measured chromium depletion profiles at longer reaction times.

Using an isothermal rate constant $k_w = 6.3 \times 10^{-12} \text{ g}^2 \text{ cm}^{-4} \text{ s}^{-1}$ and a fit of experimental weight change data to the COSP model led to an estimate of $Q_0 = 0.008$ for the one-day cycles. Breakdown was observed after 18 cycles, at which point the value $N_{\text{Cr},i} = 0.073$ was measured. Application of the combined diffusion and COSP models led to the prediction that $N_{\text{Cr},i}$ would be depleted to this level in 20 cycles, a very accurate forecast. However, the critical value of $N_{\text{Cr},i}$ was measured rather than predicted. Furthermore, the extent of transient oxidation was high, and the resulting spinel layer was observed on some occasions to spall, leaving the chromia layer more or less intact.

The phenomenon of scale delamination at phase layer boundaries has been reported a number of times, and examples are shown in Fig. 13.14. In the case of the René N5 superalloy, the outer layer was made up of transient Ni-, Co- and Cr-rich oxide remnants, together with particles of Ta-rich oxide, and the inner layer was $\alpha\text{-Al}_2\text{O}_3$. When this phenomenon is combined with occasional spallation of the inner, protective layer, the situation becomes very difficult to model.

Alumina spallation from ferritic materials and the resulting depletion of aluminium have been modelled by Quadakkers et al., as described in Section

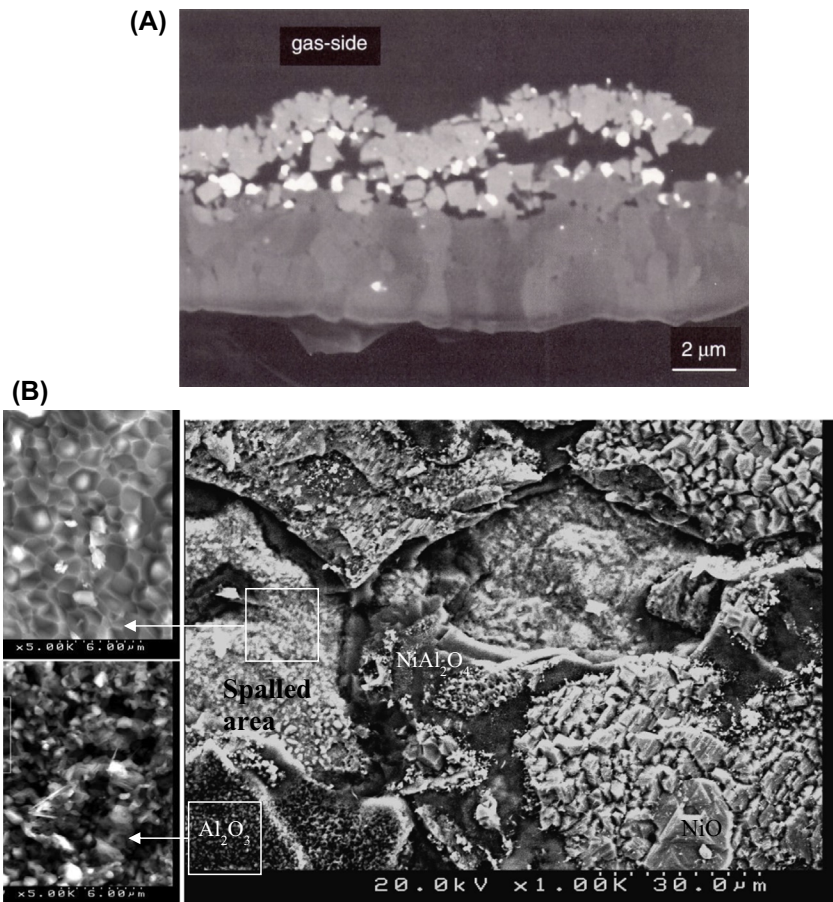


FIGURE 13.14 Spallation of scale outer layers (A) on H₂ annealed, Y-Free René N5 (B.A. Pint, P.F. Tortorelli, I.G. Wright, in Ref. 7, p. 111 with permission from IOM Communications Ltd.), (B) on γ/γ' Ni-23Al.

5.8. The situation is simplified in that case because alloy diffusion is very fast, and the depletion profiles in thin sheet materials are essentially flat.

A complete analysis of alloy depletion accompanying spallation and re healing requires an accurate description of diffusion in the subsurface alloy region. For the engineering alloys and coatings of interest, the necessary data are simply not available. Nonetheless, the models which have been developed provide a valuable predictive tool for the effect on material lifetime of varying the reaction conditions.

13.5 EFFECTS OF EXPERIMENTAL VARIABLES

13.5.1 Temperature Cycle Parameters

Several parameters are irrelevant concepts in isothermal oxidation but can be critical to the outcome of a cyclic oxidation experiment. These are the magnitude of the temperature change, ΔT , the heating and cooling rates and the cycle frequency or, equivalently, its duration. The magnitude of ΔT determines both the maximum stress (Eq. [2.168]) and, through Eq. [13.1], the maximum elastic strain energy available to fracture or spall the scale. The failure mechanism adopted by the scale depends on scale thickness [32], as does the available energy for a given ΔT . The net effect for a chromia-forming austenitic steel is shown in Fig. 13.15. It is seen that the usual experiment, which involves cooling to room temperature, will provide sufficient thermal stress to spall oxides grown at high temperature. However, the slow oxidation rates characteristic of low temperatures mean that these scales can resist thermal cycling for very long periods.

The thermally induced strain energy is only available to damage the scale if it is not dissipated by some other stress relief process. To a good approximation, this will be the case if the cooling rate is very fast. However, if it is slow, creep in the metal can reduce the stress. This effect is marked in FeCrAl

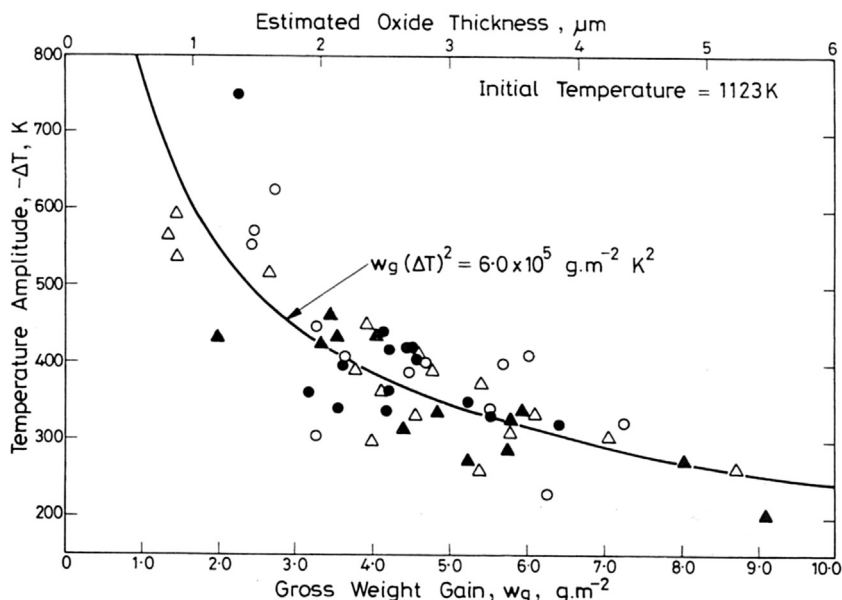


FIGURE 13.15 Critical temperature drop necessary to spall chromia from a 20Cr-25Ni Nb stabilised stainless steel. Published with permission from H.E. Evans, *Mat. Sci. Tech.* 4 (1988) 415, Maney Publishing.

materials which have low creep strength and can accommodate thermal stress to the point where their alumina scales resist spallation up to large thicknesses [5,33]. It can also be significant in materials like Haynes 214 (Ni-16Cr-3Fe-4.5Al-Y), which is a single-phase γ alloy of modest creep strength above 900°C. If cooling to this temperature is slow enough, considerable stress can be relaxed by alloy creep [34].

The effects of cycling frequency have been examined many times. According to the spallation models, shorter and more frequent cycles lead to more frequent spallation events. As shown in Eq. [13.24], this results in a smaller value of $n_{\max} \Delta t$, which therefore increases with $\Delta t^{2/3}$. As noted earlier, this predication is borne out for Ni-30Cr and the alumina former MA 956, but not for Zr-doped NiAl. However, the more important factor is subsequent metal consumption.

If, as is being assumed, the life of a material is determined by the rate of Cr or Al consumption during the final pseudo-steady-state, then Eq. [13.27] applies. This rate increases as Δt is decreased. Pint et al. [31] showed this to be qualitatively correct for the alumina formers FeCrAl, FeCrAlY, iron aluminides and undoped high sulphur content NiAl. Closer examination of the weight loss rates shown in Fig. 13.16 for ‘NiAl-1’ (Ni-50.2 at % Al, 27 ppm S) reveals average values of $-4.7 \text{ mg cm}^{-2} \text{ h}^{-1}$ during one-hour cycling, and $-1.2 \text{ mg cm}^{-2} \text{ h}^{-1}$ in 100 h cycling. The ratio between them is ca. 4:1, which compares well with the ratio predicted from Eq. [13.27] of

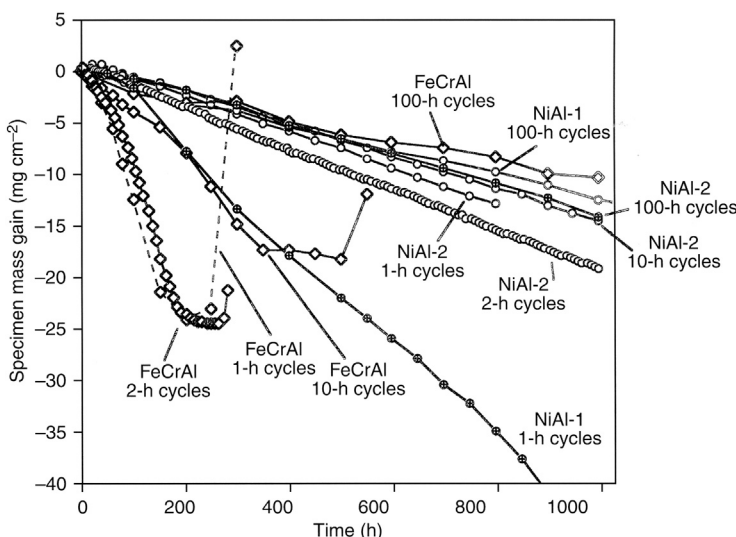


FIGURE 13.16 Specimen weight losses for undoped FeCrAl and NiAl for different cycle times at 1200°C. Published with permission from B.A. Pint, P.F. Tortorelli, I.G. Wright, in Ref. 7, p. 111, IOM Communications Ltd.

$(100/1)^{1/3} = 4.6:1$. In the case of FeCrAl, the ratio of weight loss rates observed during 2 and 100 h cycles is 5.7:1, compared with a predicted ratio of 3.7:1. This remarkable level of agreement was not reproduced by another NiAl alloy ‘NiAl-2’ (Ni-50.2 at % Al, 3 ppm S) which lost weight at essentially the same rate regardless of cycle duration. Unusual spalling behaviour of NiAl has also been reported by Smialek et al. [18,23]. Wilber et al. [7] found little difference in the spalling behaviour of FeCrAl alloys cycled for 100 and 290 h.

A reverse effect of cycle duration, ie, more rapid weight loss in longer cycles, was reported by Smialek [18] for Ni-42Al and by Pint et al. [31,35] for platinum containing NiAl and a desulphurised version of the superalloy René N5 (Appendix A). This behaviour has been rationalised [18,31] in terms of void enlargement at the scale-alloy interface during lengthy cycles. It is suggested that the development of much larger defects can lead to more extensive spallation, ie, to an increase in Q_0 . Experimental support is provided by the observations of Vialas et al. [36], who reported much larger spall fractions on NiPtAl after 6×300 h cycles than after 1800×1 h cycles. Existing spallation models cannot easily deal with such a situation, and caution should be exercised in predicting cycle frequency effects.

Finally, it should be noted that spallation resistant materials such as Hf-doped NiAl show no change in oxidation kinetics with cycle duration, at least in the early stages. This is intuitively understandable as a simple consequence of the greater strain energy (and therefore scale thickness) required to damage the much stronger scale-alloy interface. The time taken to reach a critical scale thickness for the onset of spallation is then determined by accumulated time at temperature, rather than by periodic interruptions of the scale growth process.

It is unfortunate that the currently available theory provides no reliable basis for predicting behaviour at a given cycle frequency from existing data acquired at another frequency. Current efforts [37–39] to devise a standard cyclic oxidation testing protocol are on this basis perhaps understandable. However, they will not resolve the difficulty, leaving the need to undertake additional testing programmes for new duty cycles. What is needed is an improved understanding of the way in which scale and interface mechanical properties, and defect sizes, evolve with time.

13.5.2 Continuous Thermogravimetric Analysis

Observation of oxidation kinetics and individual spallation events via CTGA provides the opportunity to validate the assumptions of the spallation models. However, the direct observation of weight loss during spallation can be complicated by apparent weight changes due to buoyancy and convection

effects. During cooling from T_1 to T_2 , the gas density increases, leading to an apparent weight decrease, δW , found from Archimedes' principle and the ideal gas equation to be

$$\delta W = \frac{MP}{R} \left(\frac{1}{T_1} - \frac{1}{T_2} \right) \quad [13.35]$$

Here M is the molar mass and P the pressure of the gas, and it has been assumed that the microbalance counterweight experiences no temperature change. Although δW can be of the same order as spallation weight change, it is easily corrected for. Convection effects are much more difficult to quantify, and it is simpler to compare the recorded weight at the beginning of a high-temperature period with the weight at the end of the preceding one, as shown schematically in Fig. 13.17. In the simplest case, heating and cooling are rapid, and the amount of oxidation occurring during the nonisothermal periods can be ignored. The total gross mass gain is obtained simply by summing the high-temperature oxygen uptake amounts, W_0 ; the spallation loss is the sum of the W_s amounts, and the net mass gain is the difference between these sums. Because W_s and the current net mass gain are available for each individual cycle, the spallation fraction k_s can be tracked through the course of the experiment. These measurements can be refined by taking into account the small amount of oxidation occurring during heating and cooling [40]. An example of the data obtainable in this way is shown in Fig. 13.18 for a nickel-based, single crystal superalloy, MC2. It is seen that k_w became approximately constant after 14 cycles. The spallation constant varied widely in the first 14

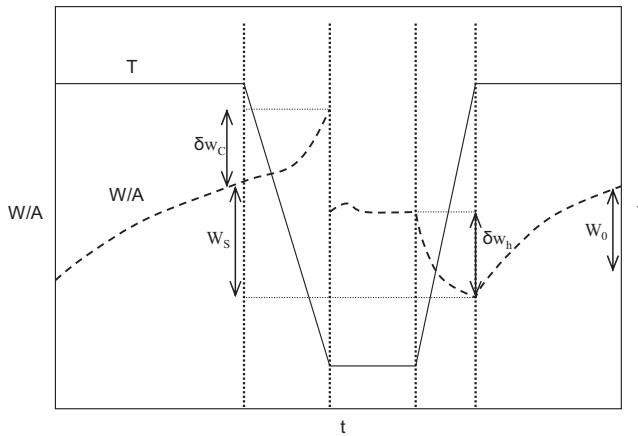


FIGURE 13.17 CTGA data from thermal cycling, showing oxidation weight gain and buoyancy changes during cooling (δw_c) and heating (δw_h) and spallation weight loss (W_s).

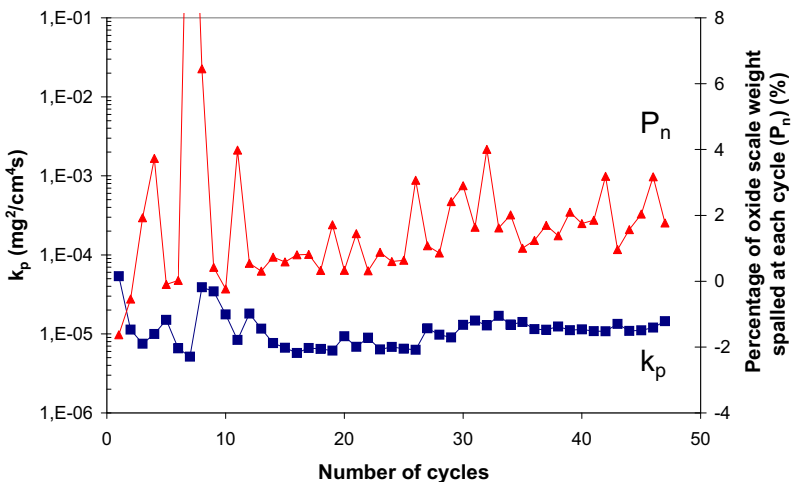


FIGURE 13.18 Evolution of instantaneous parabolic weight gain constant and spallation constant for single crystal MC2 superalloy during 15 min high-temperature cycles. *Reprinted from A. Raffaitin, D. Monceau, E. Andrieu, F. Crabos, Acta Mat. 54 (2006) 4473, with permission from Elsevier.*

cycles but then slowly increased with time over the course of this experiment, in agreement with Eq. [13.22].

Monceau et al. [27,36,40,41] and Smialek [42] have used performance ‘maps’, with spallation constant and parabolic scaling rate as axes, to compare the behaviour of different alloys and coatings. The example in Fig. 13.19 shows data for various alumina formers cycled in air at 1150°C. It shows that solute aluminium consumption by spallation increases in the order NiC-oCrAlY < NiAl < MC2. Also shown for comparison are isothermal oxidation rates for NiAl, superalloy MC2, NiCoCrAlYTa-coated superalloy and chromia formers.

13.5.3 Compositions of Alloys and Environment

Cyclic oxidation experiments have been used to study the spallation behaviour of a wide variety of chromia and alumina formers. The effects of alloy compositional variables on spallation are reviewed in Section 7.5. Most research has been concerned with cyclic exposure to air or oxygen. However, high-temperature service environments usually contain other constituents, and their effects are now considered.

Water vapour is almost always present in high-temperature service environments. As seen in Chapter 11, it can affect the growth rates of many oxide scales. Of relevance here is its effect on the volatilisation of chromia and its apparently very slight effect on isothermal alumina scaling. The cyclic

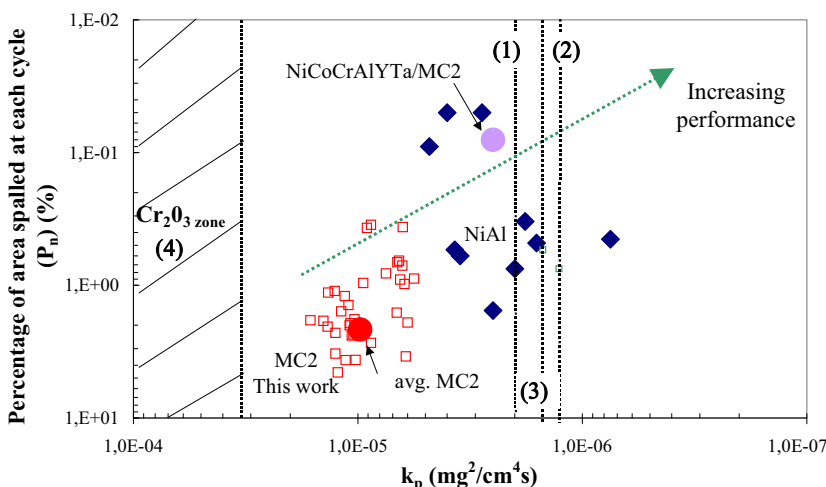


FIGURE 13.19 Spallation-oxidation map for cyclic oxidation in air at 1150°C of several alumina formers. Isothermal rate constants for NiAl (1) superalloy MC2 (2), NiCoCrAlYTa coated superalloy (3) and a range of chromia formers (4) shown for comparison. Reprinted from A. Raffaitin, D. Monceau, E. Andrieu, F. Crabos, *Acta Mat.* 54 (2006) 4473, with permission from Elsevier.

oxidation of several chromia formers in air plus H₂O(g) has been studied by Pint et al. [43–45], using lengthy cycles ($\Delta t = 100$ h) and moderate temperatures. Spallation was not significant under these conditions, and alloy performance was determined by CrO₂(OH)₂ vaporisation [46]. The situation is very different for alumina formers, because moisture can affect scale adhesion.

Smialek has reported that exposure of oxidised samples to moisture after cooling produced increased spallation from the alumina formers NiAl [18], NiCrAl [47], PWA 1480 [48], René N5 [49] and PWA 1484 [23] (Table 1.2). Sigler [50] and Smith et al. [51] have also reported that water vapour promotes alumina spallation. Controlled atmosphere thermal cycling experiments have confirmed the damaging effect of water vapour. Janakiraman et al. [52] and Maris-Sida et al. [53] compared the cyclic oxidation performance of alumina-forming, nickel-based superalloys in dry and wet ($p_{H_2O} = 0.1$ atm) air. Results in Fig. 13.20 for two PWA alloys which contained 5–8 ppm S show the accelerated spallation resulting from the presence of water vapour. Similar results were obtained for CMSX-4, a CoCrAlY coating and an aluminide coating. Subsequent work on model Ni-Al alloys (β , γ/γ' and γ) [54] and on platinum and platinum-iridium modified γ/γ' alloys [55] has demonstrated the same effect.

Materials which developed spallation-resistant alumina scales were not affected by the presence of water vapour. This is demonstrated by the behaviour of low sulphur and desulphurised PWA 1484 (Fig. 13.21) and by Hf-doped β -NiAl (Fig. 13.22). Examination confirmed that spallation was

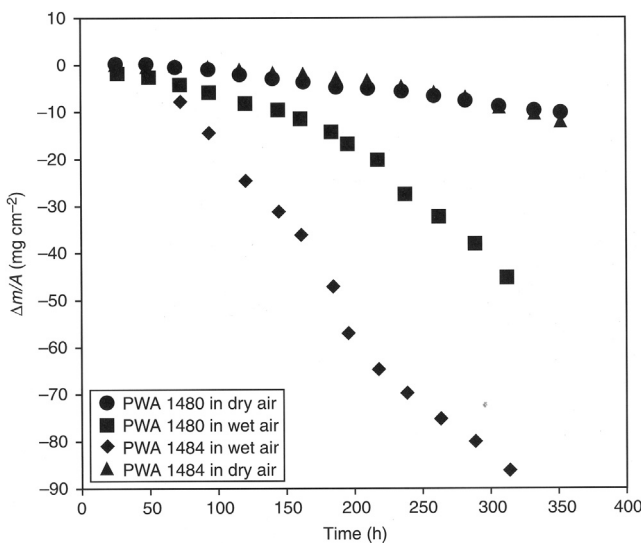


FIGURE 13.20 Effect of $p_{H_2O} = 0.1$ atm on alumina-forming superalloys exposed to 45 min oxidation cycles at 1100°C. Published with permission from R. Janakiraman, G.H. Meier, F.S. Pettit, Ref. 7, p. 38, IOM Communications Ltd.

suppressed in these cases. However, acoustic emission signals during cooling of the low sulphur PWA 1484 alloy from reaction temperature indicated that oxide cracking did occur [52]. It was therefore concluded that water vapour was able to reach the alloy surface, even when spallation did not occur.

The effect of sulphur content on nickel-base alumina-forming superalloys and on β -NiAl can be generalised as follows. In the absence of reactive elements, more than 3 ppmm S leads to scales which are poorly adherent and spallation prone. Lowering alloy sulphur levels to around 1 ppmm leads to a considerable improvement, but to realise the maximum scale adhesion, a level of ≤ 0.1 ppmm is required.

Water vapour is known [56–59] to affect the fracture behaviour of oxides, including α - Al_2O_3 . The polar water molecule is thought to attach to Al-O bonds at a crack tip, weakening those bonds and in effect reducing the fracture toughness of the oxide. Meier et al. [52,53] propose that a similar phenomenon could occur at the alloy-alumina interface. When sulphur is present in the alloy, it segregates to the scale-metal interface, decreasing its toughness. Water vapour decreases the interfacial toughness even more, and oxide spallation is promoted. When sulphur is not present to weaken the interface, or when hafnium is added to strengthen the interface, the water vapour effect is prevented. Either the water molecules cannot access the interface (even though the oxide is cracked) or the interfacial toughness is so high that any weakening caused by water is insufficient to cause spallation.

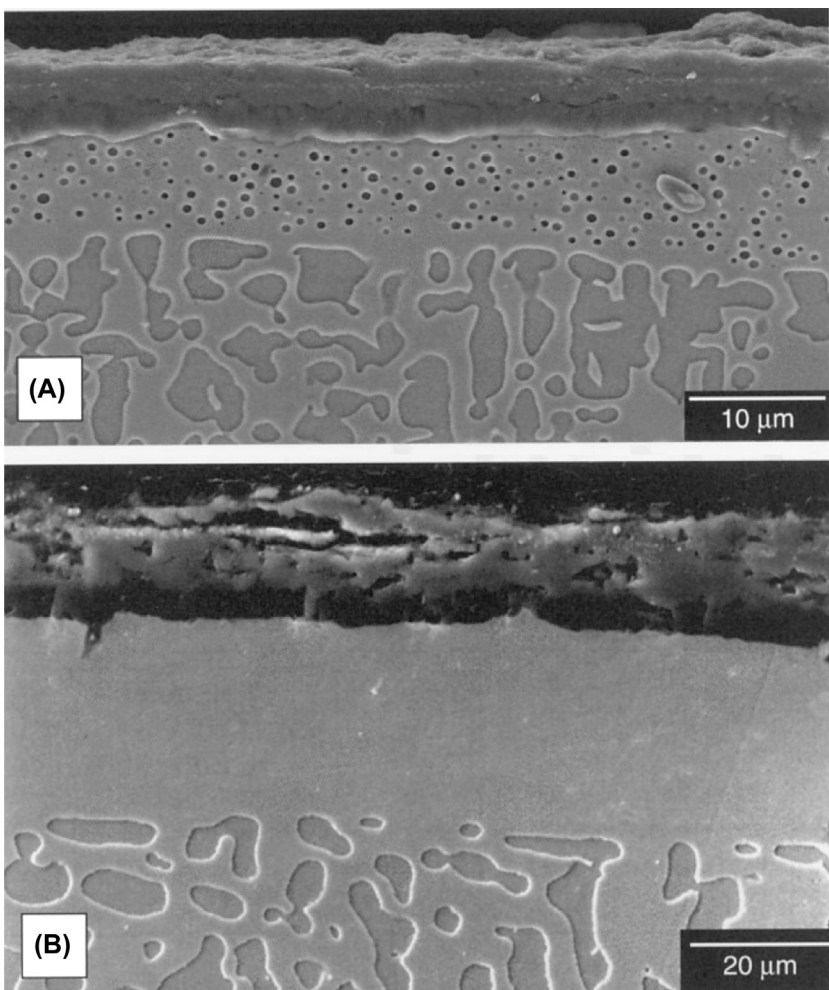


FIGURE 13.21 Appearance after cyclic oxidation of desulphurised PWA 1484 in (A) dry and (B) wet ($p_{\text{H}_2\text{O}} = 0.1 \text{ atm}$) air, 45 min cycles at 1100°C . Published with permission from R. Janakiraman, G.H. Meier, F.S. Pettit, Ref. 7, p. 38, IOM Communications Ltd.

Alloy breakdown can result from internal precipitation reactions as well as the more usually discussed external oxidation of alloy solvent metals. The development of internal oxidation during cyclic reaction has been reported several times [60–64]. The presence in the gas of secondary oxidants can exacerbate this situation if the other oxidant has a greater permeability in the alloy than oxygen. Both nitrogen and carbon have higher permeabilities than oxygen in austenite (Table 6.2) and are therefore potential threats to the long-term performance of heat-resistant steels and nickel-base alloys. The ability of

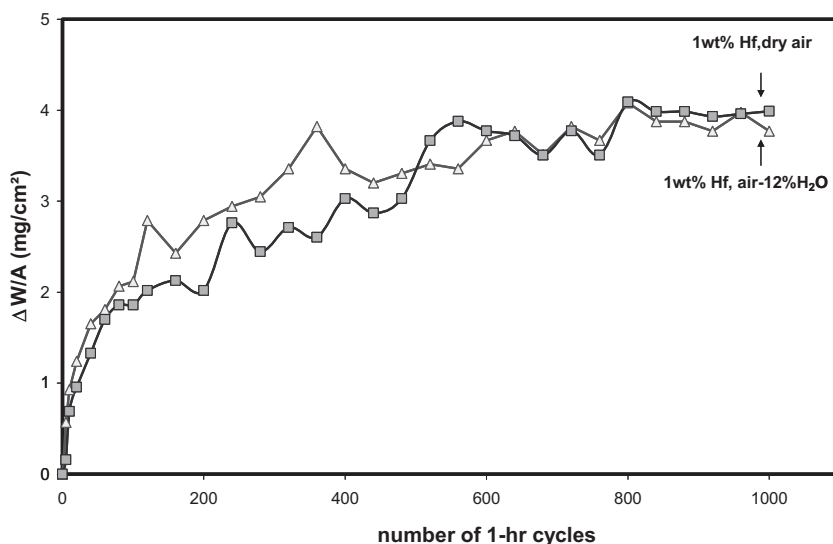
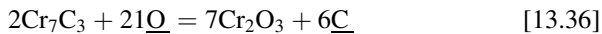


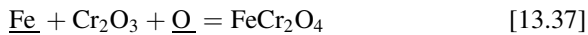
FIGURE 13.22 Cyclic oxidation at 1200°C (one-hour cycles) of β -NiAl with Hf doping in dry and wet air ($p_{\text{H}_2\text{O}} = 0.1 \text{ atm}$).

an alloy to reform a protective oxide scale after spallation can be determined not simply by the depletion phenomena discussed in Sections 13.2 and 13.4, but by the competition between outward diffusion of a scale-forming metal and inward diffusion of a secondary oxidant. Internal precipitation of the scale-forming metal as nitride or carbide immobilises it, effectively causing more severe depletion.

As discussed in Chapter 9, carbon attacks heat-resisting alloys very rapidly, causing deep carburisation and, in some atmospheres, metal dusting. Cyclic exposure [65] of 304 stainless, Alloy 800 and 602CA (Table 9.1) to CO/CO₂ atmospheres which were both oxidising and carburising to chromium led to the reaction morphologies shown in Fig. 13.23. The two chromia-forming alloys failed, suffering extensive internal precipitation. The reaction of 304 stainless was the more complex, forming multiple internal precipitation zones. Chromium-rich carbides precipitated deep within the alloy, and an internal oxidation front advanced into the alloy behind the carburisation front as the in situ oxidation of internal carbide



continued. Subsequent spinel formation at the even higher oxygen potentials near the alloy surface



developed an additional internal precipitation zone (Section 6.9). The sequence of zones reflects the relative stabilities of the precipitates, and the

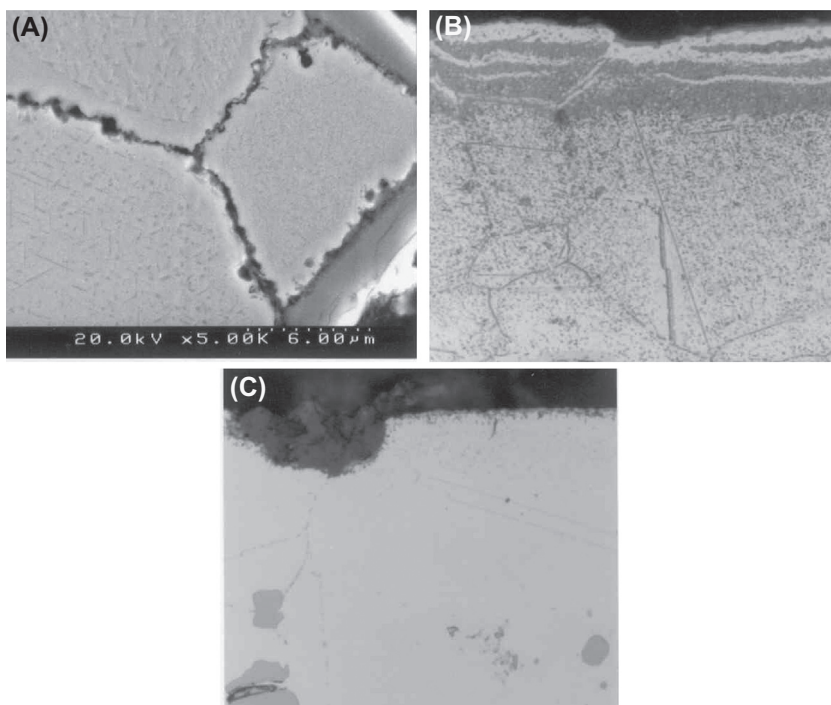


FIGURE 13.23 Heat-resisting alloys after exposure to CO/CO₂ mixtures for 520 cycles at 700°C
 (A) alloy 800 (B) 304 stainless (C) 602 CA. Reprinted from M. Hansel, C. Boddington, D.J. Young, *Corros. Sci.* 45 (2003) 967 with permission from Elsevier.

faster diffusion of carbon. Alloy 602CA, which is a marginal alumina former, resisted carbon attack.

As seen in [Fig. 13.23](#), very large oxide volume fractions resulted, causing significant expansion and disruption of the alloy surface. The magnitude of these effects can be estimated from precipitate species molar volumes on the assumption that all chromium is precipitated. Results are shown in [Table 13.3](#).

TABLE 13.3 Calculated Effects of Complete Internal Chromium Precipitation in 304 Stainless Steel

Precipitate	f_v	$\Delta V (\%)$
FeCr ₂ O ₄	0.45	40
Cr ₂ O ₃	0.32	21
Cr ₇ C ₃	0.21	3
Cr ₂₃ O ₆	0.20	3

The mechanical stress associated with these large volume changes would have been exacerbated by thermal cycling, leading to the observed alloy disintegration. The role of carbon in producing this effect is critical. Such large quantities of internal oxide cannot normally form, an external scale developing instead. It was the prior internal carburisation resulting from thermal cycling-induced scale spallation which allowed subsurface oxide formation via reaction Eqs [13.36] and [13.37]. Thermal cycling in other oxidising-carburising environments can be used to accelerate protective scale failure, and the onset of metal dusting attack [66].

The permeability of nitrogen in austenite is not as high as that of carbon, but it is sufficient to accelerate internal attack of an alloy depleted by successive spallation-rehealing events. Thermal cycling in air can lead to the development of multizone internal precipitation regions beneath the surface, with nitrides located at greater depths than oxides [9,67,68]. This phenomenon may be more frequent than has been reported for air oxidation, because the nitrides can be difficult to distinguish metallographically from oxides (Fig. 13.24). Internal precipitation kinetics are complex, as shown in Fig. 13.24B, with initially parabolic behaviour followed by linear penetration. It has been suggested [60,68] that the large internal precipitate volumes, coupled with cyclic thermal expansion and contraction, lead to cracking and gas access to the alloy interior.

Results obtained for cyclic corrosion in sulphur-bearing environments are complex. Laboratory hot corrosion tests (Section 8.8) often involve periodic addition of salt to sample surfaces. This is usually done at time intervals which are some multiple of Δt . Leyens et al. [69] have reported that the frequency (and rate) of salt addition is an important variable, the corrosion rate of NiCoCrAlY alloys increasing with less frequent but larger salt additions. Decomposition and evaporation of the sulphate salts was clearly involved, but the interaction between oxide spallation, corrosion and salt weight changes made kinetic data difficult to interpret.

As seen in Chapter 8, corrosion by reducing sulphidising gases is particularly severe. The only practical way of protecting alloys against such gases is by forming oxide scales capable of surviving at low oxygen activities. The ability of these alloy-scale systems to resist spallation and to reheat after damage is then of critical importance. Cyclic exposure experiments [70] have been used to explore the behaviour of ferritic and austenitic steels in sulphidising-oxidising gases at 600°C. Despite the relatively low temperature, thick scales were formed. However, the low temperature and slow rate of temperature change in the autoclave used in these experiments led to only small degrees of spallation.

Weber and Schutze [71] subjected thermal spray coatings of Ni–48 Al–1.5Cr (at. %), TiAl and TiSi₂ on a low alloy steel and a ferritic 18Cr-1Al steel to cyclic exposure in Ar-5%H₂-1%H₂S at 700°C. Impurity amounts of H₂O(g) made the gas oxidising to aluminium and silicon, but borderline

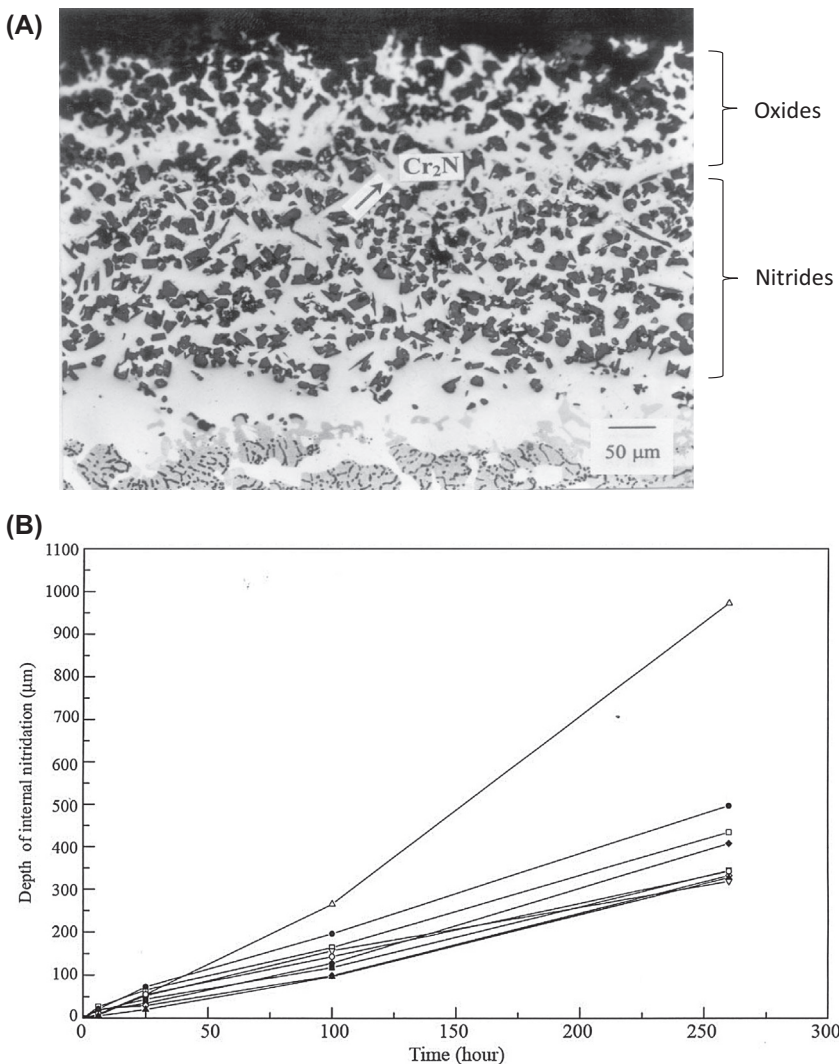


FIGURE 13.24 Internal oxidation and nitridation of $\alpha + \beta + \gamma$ -phase Ni-Cr-Al alloys produced by thermal cycling in air at 1100°C (260 one-hour cycles): (A) reaction morphology in Ni-30Cr-20Al (fragmentary outer oxide scale present but not visible) and (B) internal nitridation kinetics for different three-phase alloys.

sulphidising-oxidising to titanium. The porous nature of spray deposited coatings can render them gas permeable. Although oxidation tends to fill the pore space, sulphides also form, and internal sulphidation of the substrate steels results. The presence of nickel was disadvantageous, and the TiAl and TiSi_2 coatings provided better performance. The thermal cyclic

performance of dense, aluminium-rich materials in sulphidising gases might be interesting.

13.6 DESCRIBING AND PREDICTING CYCLIC OXIDATION

Cyclic oxidation experiments combine high-temperature reaction with the mechanical effects of thermally induced stress on protective scales, providing a realistic simulation of high-temperature service. This is particularly so if controlled gas atmospheres are used to reproduce service conditions.

Modern alloys and coatings provide superior resistance to cyclic oxidation and designing efficient laboratory test programmes is a challenge. One approach is simply to test for long times, two years or more [64,72,73], until depletion of the protective scale-forming metal leads to breakaway oxidation. It is obviously desirable to be able to accelerate the experiments to reduce costs and speed the introduction of new materials. As we have seen, alloy degradation is accelerated by increasing temperature to speed the corrosion reaction and by shortening the cycles to increase spalling frequency. However, this is useful only if a reliable method exists for extrapolating the laboratory test results to the service conditions of interest. For this very practical reason, we are interested in the use of modelling to arrive at an accurate description and a method of prediction for spallation-induced alloy depletion.

The diffusion model for alloy depletion accompanying scale spallation and rehealing is well-developed. Based on the interaction between the depletion process of selective oxidation and the replenishment process of alloy diffusion, it describes the balance in terms of the ratio $\varphi = (\pi k_c / 2\tilde{D})^{1/2}$. When combined with a realistic description of spallation extent, it can provide reasonable lifetime predictions. However, it succeeds only to the extent allowed by the accuracy and completeness of the data available for diffusion in the substrate alloy. In the case of Fe-Cr-Al alloys, which have very high diffusion coefficients at their typical operating temperatures, the depleted profile in N_{Al} is adequately approximated as being flat in thin sections, and predictions of lifetimes can work well. However, diffusion in the commonly used austenitic heat-resisting alloys, in superalloys and in coating materials is slower, and varies in a complex way with composition. Available data are generally insufficient to justify calculations. However, this shortcoming can be overcome by the expedient of measuring average interdiffusion coefficients and the critical interface concentration, $N_{B,i}$, of scale-forming metal required, at both the service and laboratory test temperatures.

The spallation models examined in this chapter succeed in describing the general form of experimentally observed weight change kinetics. They also achieve quantitative success in relating the number of cycles required to reach the maximum weight uptake with the number at which the net weight change becomes negative and, most importantly, the ultimate constant rate of weight

loss, and therefore depletion. With this degree of success, we might hope that the models would allow the all-important prediction of the effects on lifetime of changing temperature and cycling frequency. Unfortunately, the empirical nature of models which treat spallation probability as an adjustable parameter permit no such thing.

The essence of the problem is that spallation is treated as a random event, unrelated to experimental variables other than through Eq. [13.1]. It is therefore not possible to predict the effect of changing temperature on the spallation fraction (ie, probability) without recourse to other fracture mechanics-based descriptions. These are numerous, reflecting the diversity of mechanisms available for the initiation and propagation of fast fracture in scale-substrate systems. It seems likely that the temperature effect on k_s will be strongly dependent on the alloy-gas system involved, and more information is required.

Spallation-induced weight loss changes are predicted to change at a given temperature and constant value of k_w , with cycle frequency in a simple way. However, while the expected dependency of final weight loss rate on $(\Delta t)^{-1/3}$ is found for a number of materials, for others it is not. One reason for this failure is the overly simplistic nature of the assumed oxidation morphology, that of a single-phase external scale. The real situation is much more complex. Remnant transient oxides (Section 5.7) form an outer layer which can spall, causing weight loss, but leave the protective function of the underlying alumina or chromia unimpaired. As the concentration of the primary scale-forming metal is lowered, additional layers of spinel develop at the scale surface, altering the observed weight change rates. Finally, we note that depletion of an alloy often renders it susceptible to internal oxidation or attack by a secondary corrodent (Chapter 6), complicating still further the cyclic weight change behaviour. No model descriptions are available for the effect on cyclic weight change kinetics of these more complex reaction morphologies.

REFERENCES

- [1] U.R. Evans, An Introduction to Metallic Corrosion, Arnold, London, 1948.
- [2] H.E. Evans, R.C. Lobb, Corros. Sci. 24 (1984) 209.
- [3] M.I. Manning, in: V. Guttman, M. Merz (Eds.), Corrosion and Mechanical Stress at High Temperatures, Applied Science, London, 1981, p. 323.
- [4] H.E. Evans, G.P. Mitchell, R.C. Lobb, D.R.J. Owen, Proc. Roy. Soc. London A440 (1993) 1.
- [5] H.E. Evans, Int. Mater. Rev. 40 (1995) 1.
- [6] M. Schutze, Protective Oxide Scales and Their Breakdown, John Wiley and Sons, Chichester, 1991.
- [7] J.P. Wilber, M.J. Bennett, J.R. Nicholls, in: M. Schutze, W.J. Quadakkers (Eds.), Cyclic Oxidation of High Temperature Materials, IOM Communications, London, 1999, p. 133.
- [8] J.C. Pivin, D. Delauney, R. Roques-Carmes, A.M. Huntz, P. Lacombe, Corros. Sci. 20 (1980) 351.
- [9] S.Y. Chang, U. Krupp, H.J. Christ, in Ref. 7, p. 63.

- [10] U. Krupp, S.Y. Chang, A. Schimke, H.J. Christ, in: M. Schutze, W.J. Quadakkers, J.R. Nicholls (Eds.), *Lifetime Modelling of High Temperature Corrosion Processes*, Maney Publishing, London, 2001, p. 148.
- [11] P. Vangeli, Ref. 7, p. 198.
- [12] J.-C. Salabura, D. Monceau, *Mater. Sci. Forum* 461–464 (2004) 689.
- [13] D. Monceau, D. Poquillon, *Oxid. Met.* 61 (2004) 143.
- [14] D.P. Whittle, *Oxid. Met.* 4 (1972) 171.
- [15] D.P. Whittle, *Acta Met.* 17 (1969) 1729.
- [16] J.A. Nesbitt, *J. Electrochem. Soc.* 136 (1989) 1518.
- [17] G. Wahl, *Thin Solid Films* 107 (1983) 417.
- [18] J.L. Smialek, *Met. Trans. A* 9A (1978) 309.
- [19] C.E. Lowell, J.L. Smialek, C.A. Barrett, in: R.A. Rapp (Ed.), *High Temperature Corrosion*, NACE, Houston, TX, 1983, p. 219.
- [20] H.B. Probst, C.E. Lowell, *J. Metals* 40 (1988) 18.
- [21] C.E. Lowell, C.A. Barret, R.W. Palmer, J.V. Auping, H.B. Probst, *Oxid. Met.* 36 (1991) 81.
- [22] J.L. Smialek, J.V. Auping, *Oxid. Met.* 57 (2002) 559.
- [23] J.L. Smialek, J.A. Nesbitt, C.A. Barrett, C.E. Lowell, Ref. 7, p. 148.
- [24] J.A. Nesbitt, C.A. Barrett, in: R. Darolia (Ed.), *Structural Intermetallics*, TMS-AIME, Warrendale, PA, 1993, p. 601.
- [25] P.W. Simpson, H.E. Evans, *Nuclear Fuel Performance*, vol. 1, British Nuclear Energy Society, London, 1985.
- [26] K.S. Chan, *Met. Mat. Trans. A* 28A (1997) 411.
- [27] D. Poquillon, D. Monceau, *Oxid. Met.* 59 (2003) 409.
- [28] J.A. Nesbitt, R.W. Heckel, *Oxid. Met.* 29 (1988) 75.
- [29] C.A. Barrett, C.E. Lowell, *Oxid. Met.* 11 (1977) 199.
- [30] B. Li, B. Gleeson, *Oxid. Met.* 65 (2006) 101.
- [31] B.A. Pint, P.F. Tortorelli, I.G. Wright, in Ref. 7, p. 111.
- [32] H.E. Evans, *Mat. Sci. Tech.* 4 (1988) 415.
- [33] H.E. Evans, *Mater. High Temp.* 12 (1994) 219.
- [34] H.E. Evans, Ref. 7, p. 3.
- [35] B.A. Pint, I.G. Wright, W.Y. Lee, Y. Zhang, K. Prussner, K.B. Alexander, *Mater. Sci. Eng. A245* (1998) 201.
- [36] N. Vialas, D. Monceau, B. Pieraggi, *Mater. Sci. Forum* 461–464 (2004) 747.
- [37] J.R. Nicholls, M.J. Bennett, Ref. 7, p. 437.
- [38] http://www.iso.org/iso/home/store/catalogue_tc/catalogue_detail.htm?csnumber=53992.
- [39] S. Osgerby, R. Petterson, *Mater. Corros.* 57 (2006) 14.
- [40] A. Raffaitin, D. Monceau, E. Andrieu, F. Crabos, *Acta Mat.* 54 (2006) 4473.
- [41] D. Poquillon, D. Monceau, in: *Proc. TMS Annual Meeting*, San Diego, 2003, p. 165.
- [42] J. Smialek, *Acta Mater.* 52 (2004) 2111.
- [43] B.A. Pint, ASME Paper# GT2005-68495, New York, in: *International Gas Turbine & Aeroengine Congress*, Barcelona, May 2006, 2005.
- [44] B.A. Pint, *J. Eng. Gas Turbines and Power* 128 (2006) 370.
- [45] R. Peraldi, B.A. Pint, *Oxid. Met.* 61 (2004) 463.
- [46] D.J. Young, B.A. Pint, *Oxid. Met.* 66 (2006) 137.
- [47] J.L. Smialek, in: M.A. Dayananda, S.J. Rothman, W.E. King (Eds.), N.L. Peterson Memorial Symposium, *Oxidation of Metals and Associated Mass Transport*, TMS-AIME, Warrendale PA, 1987, p. 297.

- [48] B.K. Tubbs, J.L. Smialek, in: V. Srinivasan, K. Vedula (Eds.), Corrosion and Particle Erosion at High Temperatures, TMS-AIME, Warrendale PA, 1989, p. 459.
- [49] J.L. Smialek, D.T. Jayne, J.C. Schaeffer, W.H. Murphy, Thin Solid Films 253 (1994) 285.
- [50] D.R. Sigler, Oxid. Met. 40 (1993) 555.
- [51] M.A. Smith, W.E. Frazier, B.A. Pregger, Mater. Sci. Eng. A203 (1995) 388.
- [52] R. Janakiraman, G.H. Meier, F.S. Pettit, Ref. 7, p. 38.
- [53] M.C. Maris-Sida, G.H. Meier, F.S. Pettit, Met. Trans. A 34A (2003) 2609.
- [54] R. Kartono, D.J. Young, in: E. Opila, J. Fergus, T. Maruyama, J. Mizusaki, T. Narita, D. Schiffler, E. Wachima (Eds.), High Temp. Corros. Mater. Chem. V, The Electrochemical Society, Pennington NJ, 2005, p. 43.
- [55] R. Kartono, D.J. Young, Mater. Corros. 59 (2008) 455.
- [56] S.M. Weiderhorn, J. Am. Ceram. Soc. 50 (1967) 407.
- [57] S.M. Weiderhorn, Int. J. Fract. Mech. 4 (1968) 171.
- [58] T.A. Michalski, S.W. Freiman, J. Am. Ceram. Soc. 66 (1983) 284.
- [59] T.A. Michalski, S.W. Freiman, B. Bunker, Am. Ceram. Soc. Bull. 61 (1982) 414.
- [60] W. Cheung, B. Gleeson, D.J. Young, Corros. Sci. 35 (1993) 923.
- [61] D. Prajtno, B. Gleeson, D.J. Young, Corros. Sci. 39 (1997) 639.
- [62] M.A. Harper, J.E. Barnes, G.Y. Lai, Corrosion 97 (1997). Paper No. 132, NACE, Houston TX.
- [63] B. Gleeson, M.A. Harper, Oxid. Met. 49 (1998) 373.
- [64] M.A. Harper, B. Gleeson, Ref. 7, p. 273.
- [65] M. Hansel, C. Boddington, D.J. Young, Corros. Sci. 45 (2003) 967.
- [66] C.H. Toh, P.R. Munroe, D.J. Young, K. Fogar, Mater. High. Temp. 20 (2003) 129.
- [67] U. Krupp, H.-J. Christ, Oxid. Met. 52 (1999) 277.
- [68] S. Han, D.J. Young, Oxid. Met. 55 (2001) 225.
- [69] C. Leyens, I.G. Wright, B.A. Pint, P.F. Tortorelli, Ref. 7, p. 169.
- [70] M. Maier, J.F. Norton, Ref. 7, p. 240.
- [71] T. Weber, M. Schutze, Ref. 7, p. 259.
- [72] D. Naumenko, L. Singheiser, W.J. Quadakkers, in: M. Schutze, W.J. Quadakkers (Eds.), Cyclic Oxidation of High Temperature Materials, IOM Communications, London, 1999, p. 287.
- [73] A. Aguero, R. Muelas, M. Gutierrez, R. Van Vulpen, S. Osgerby, J.P. Banks, Surf. Coat. Tech. 201 (2007) 6253.